

Article

Characterizing Extreme Events in a Fabry–Perot Laser with Optical Feedback

Shanshan Ge ^{1,2}, Yu Huang ^{1,2,*}, Kun Li ^{1,2}, Pei Zhou ^{1,2} , Penghua Mu ³, Xin Zhu ^{1,4} and Nianqiang Li ^{1,2,*}

¹ School of Optoelectronic Science and Engineering, Soochow University, Suzhou 215006, China; 20215239038@stu.suda.edu.cn (K.L.); peizhou@suda.edu.cn (P.Z.)

² Key Lab of Advanced Optical Manufacturing Technologies of Jiangsu Province & Key Lab of Modern Optical Technologies of Education Ministry of China, Soochow University, Suzhou 215006, China

³ Institute of Science and Technology for Opto-Electronic Information, Yantai University, Yantai 264005, China

⁴ Matrix Opto. Co., Ltd., Zhangjiagang 215614, China

* Correspondence: yhuang12@suda.edu.cn (Y.H.); nli@suda.edu.cn (N.L.)

Abstract: The study of extreme events (EEs) in photonics has expanded significantly due to straightforward implementation conditions. EEs have not been discussed systematically, to the best of our knowledge, in the chaotic dynamics of a Fabry–Perot laser with optical feedback, so we address this in the current contribution. Herein, we not only find EEs in all modes but also divide the EEs in total output into two categories for further discussion. The two types of EEs have similar statistical features to conventional rogue waves. The occurrence probability of EEs undergoes a saturation effect as the feedback strength increases. Additionally, we analyze the influence of feedback strength, feedback delay, and pump current on the probability of EEs defined by two criteria of EEs and find similar trends. We hope that this work contributes to a deep understanding and serves as inspiration for further research into various multimode semiconductor laser systems.

Keywords: extreme event; chaotic; multimode; semiconductor laser; optical feedback



Citation: Ge, S.; Huang, Y.; Li, K.; Zhou, P.; Mu, P.; Zhu, X.; Li, N. Characterizing Extreme Events in a Fabry–Perot Laser with Optical Feedback. *Photonics* **2024**, *11*, 462. <https://doi.org/10.3390/photonics11050462>

Received: 21 April 2024

Revised: 10 May 2024

Accepted: 13 May 2024

Published: 15 May 2024



Copyright: © 2024 by the authors. Licensee MDPI, Basel, Switzerland. This article is an open access article distributed under the terms and conditions of the Creative Commons Attribution (CC BY) license (<https://creativecommons.org/licenses/by/4.0/>).

1. Introduction

For centuries, sailors have been telling stories of rogue waves appearing without warning in the deep sea [1]. The waves, which are as high as mountains, are known to destroy or engulf ships in an instant and then disappear without a trace. Early, rogue waves only attracted the attention of the oceanographic community, and people hoped that measures could be taken to reduce the loss after understanding the mechanism of such catastrophic phenomena. Later, similar concepts were extended to other fields, including tsunamis, earthquakes, supernovae, stock markets [2–5], etc. Rogue waves in optics are also known as extreme events (EEs), specifically referring to the sudden occurrence of high-amplitude pulses [6,7]. In 2007, Solli et al. compared the propagation of light fields in fibers with the occurrence of rogue waves in the ocean and proposed the concept of optical EEs, which opened a new field of research on EEs in optical systems [8–13].

In recent years, chaotic semiconductor lasers have been used as platforms for understanding, predicting, and controlling EEs due to their fast dynamic characteristics, miniaturization, and ease of manipulation. The research on EEs in various chaotic semiconductor lasers is widely carried out. For example, Bosco et al. investigated EEs in edge-emitting diode lasers with phase-conjugate feedback and revealed the time interval between two EEs following two Poisson laws with different slopes [14]. Spitz et al. first observed EEs in mid-infrared emitting quantum cascade lasers (the emitting wavelength is 5.6 μm) with external optical feedback and obtained a pulse with controlled spacing by adding a periodic modulation of the pumping current, which provides a possibility to implement photonic biological neurons [15]. Coulibaly et al. monitored EEs emerging in deterministic spatiotemporal chaos from a quasi-1D broad-area laser with a saturable

absorber [16]. This study demonstrated how spatiotemporal extended intermittency induces the generation of extreme events. Furthermore, Masoller et al. observed some high-amplitude pulses in the deterministic nonlinearity based on an optically injected vertical cavity surface emitting laser (VCSEL) [17], in which the probability density function emerges with a long tail. More interestingly, Uy et al. found two types of EEs, i.e., vectorial and scalar EEs, separately corresponding to the emission of EE in both linear polarizations simultaneously and in single linear polarization, in the polarization dynamics of VCSELs with optical feedback [18]. After introducing the spin degrees of freedom, Zeng et al. also detected a new EE that only appears in total intensity in a free-running spin-VCSEL [19]. The exploration of EEs in multiple polarization chaotic semiconductor lasers significantly advances their related fields.

In this paper, we numerically investigate the occurrence and evolution of EEs in the chaotic output of a multimode Fabry–Perot (FP) laser with optical feedback. Benefiting from multiple longitudinal lasing modes, Fabry–Perot lasers have been widely investigated in different fields such as reinforcement learning [20], reservoir computing [21], secure communications [22], and biological neurons [23]. As we know, the appearance of EEs in the chaotic output may degrade the performance of the chaos-based applications mentioned above. Given this, we here select an external-cavity FP laser as the chaotic source, explore the possibility for EE appearance, and then analyze the evolution of EEs under various parameter settings. Specifically, we classify the EEs in the total and individual mode output and study their properties by varying several experimentally controllable parameters, i.e., feedback strength, feedback delay, and pump current, in virtue of two EE criteria.

2. Theoretical Model

Based on expanding Lang-Kobayashi equations [24], an FP laser subjected to optical feedback can be described as [25,26]:

$$\frac{dE_m(t)}{dt} = \frac{1}{2}(1 + i\alpha) [G_m(t) - \gamma_p] E_m(t) + k_f E_m(t - \tau_f) \exp(-i\omega_m \tau_f), \quad (1)$$

$$\frac{dN(t)}{dt} = \frac{I}{e} - \gamma_e N(t) - \sum_{m=1}^M G_m(t) |E_m(t)|^2, \quad (2)$$

$$\frac{dN(t)}{dt} = \frac{I}{e} - \gamma_e N(t) - \sum_{m=1}^M G_m(t) |E_m(t)|^2, \quad (3)$$

where the subscript m represents the mode number, M denotes the total number of the longitudinal mode, and the central mode is designated as $m_c = 3$. $E(t)$ is the complex electric field amplitude, $N(t)$ is the carrier number, $G_m(t)$ is the mode-dependent optical gain, $\Delta\omega_L = 2\pi/\tau_L$ is the longitudinal mode spacing, τ_L is the round-trip time of light in an external cavity, $\omega_m = \omega_c + (m_c - m)\Delta\omega_L$ is the angle frequency, $\Delta\omega_g$ is the gain width of the laser material, α is the linewidth enhancement factor, γ_p is the photon decay rate, γ_e is the carrier decay rate, I is the pump current, s is the saturation compression factor, g is the differential gain coefficient, and N_0 is the transparency inversion. The last term of Equation (1) illustrates the optical feedback effect, where the feedback parameters include the feedback strength k_f and the feedback delay τ_f .

The above differential equations are solved by the fourth-order Runge-Kutta algorithm with a time step of 1 ps [27], according to the parameter setting in Refs. [25,26]: $\alpha = 3.5$, $\gamma_p = 0.238 \text{ ps}^{-1}$, $\gamma_e = 0.621 \text{ ns}^{-1}$, $I_{th} = 19.8 \text{ mA}$, $\tau_L = 8.5 \text{ ps}$, $\Delta\omega_g = 2\pi \times 10 \text{ THz}$, $s = 1 \times 10^{-7}$, $g = 3.2 \times 10^{-9} \text{ ps}^{-1}$, $N_0 = 1.25 \times 10^8$, $M = 5$. Our simulations are performed with a time duration of 11 μs , and the relative number of EEs is calculated in the last 10 μs . To quantitatively distinguish EEs from all events, two common criteria are employed. One definition is the abnormality index (AI). The AI of event n can be defined as $AI_n = Hf_n/H_{1/3}$, where Hf_n is the difference between the peak height of the event and the mean height of all events in the time series and $H_{1/3}$ is the average value of the first

third of the highest values of Hf_n . Any event that yields an abnormality index greater than 2 is considered an EE [14,28–31]. Another threshold is defined as the average height of pulses, $\langle H \rangle$, plus 5 times the standard deviation of the distribution of pulse height, σ . If the height of an event exceeds the threshold, it is identified as an EE [29,31].

Moreover, we define the dominant mode ratio as the ratio of the dominant mode of mode m over a long period. The dominant mode ratio DMR_m for mode m is as follows [26]:

$$DMR_m = \frac{1}{k} \sum_{j=1}^k D_m(j) \tag{4}$$

where k stands for the total number of sample points corresponding to the time length. $D_m(j) = 1$ when the intensity of mode m becomes dominant (the largest intensity among all the modes) at the j -th sampling point, and $D_m(j) = 0$ otherwise.

3. Results and Discussion

3.1. Threshold Defined by the Abnormality Index

To begin with, we present a bifurcation diagram of the total intensity $I_{total} = I_{M1} + I_{M2} + I_{M3} + I_{M4} + I_{M5}$ of the FP laser with optical feedback (we place an optical fiber mirror in front of the cavity of a free-running laser and cause the light field to be reflected back into the cavity), as shown in Figure 1a. The corresponding results of the 0-1 test for chaos (magenta line) and the threshold of $AI = 2$ (red line) are also plotted in Figure 1a. In fact, the bifurcation results for I_{total} , I_{M1} , I_{M2} , I_{M3} , I_{M4} , and I_{M5} are similar; therefore, only the total intensity I_{total} is displayed. Figure 1a illustrates that the FP laser follows the quasiperiodic dynamics of the chaos routine as the feedback strength increases. Moreover, we display time series for the stable state, periodic (pulsing) state, and chaotic state in Figure 1(b1), Figure 1(b2), and Figure 1(b3), respectively. From Figure 1a, one can find some extrema occurring above the red line of the EE threshold we defined, which means that EEs are triggered over a wide range of feedback strengths. This region typically exhibits chaotic dynamics, as indicated by 0–1 test results approaching 1.

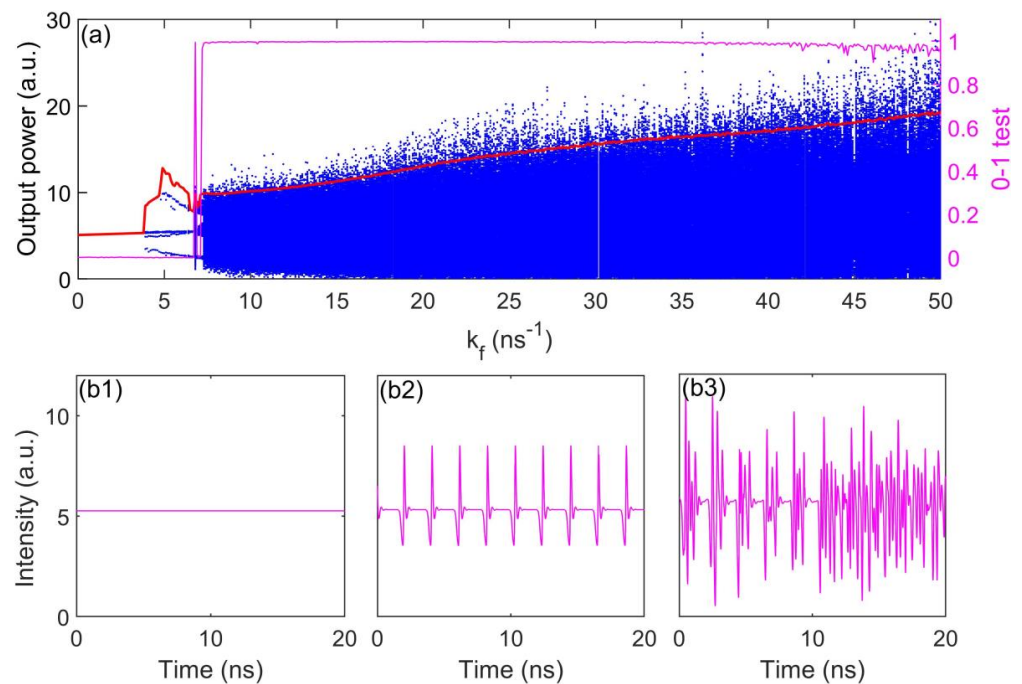


Figure 1. (a) Bifurcation diagrams plotting extrema of the total intensity and the corresponding results of the 0-1 test for chaos (the magenta line), where $\tau_f = 2$ ns. (b) Intensity time series, where (b1) $k_f = 3$ ns⁻¹, (b2) $k_f = 4$ ns⁻¹, and (b3) $k_f = 10$ ns⁻¹. The red line is the threshold of $AI = 2$.

Next, we plot the typical chaotic time series of the FP laser in Figure 2(a1,a2), where different colors correspond to different mode outputs and the dashed lines stand for the threshold of $AI = 2$ in the corresponding time series. In this figure, we find that many pulses in the chaos exceed the threshold and are thus strong enough to be considered as EEs in all modes. Figure 2(b1,b2,c1,c2) display zooms of the time series of I_{total} and $I_{M1,M2,M3,M4,M5}$ with the EEs, marked by colored squares. Notably, we find an interesting phenomenon where an EE occurs in I_{total} , and simultaneously (their time separation is below 30 ps) an EE may be triggered in the dominant mode. Here we give the classification criteria for the following discussion: When an EE is only triggered in the total intensity but not in the dominant mode, we classify it as type 1, as shown in Figure 2(b1,b2). In contrast, if an EE is triggered in both the total intensity and the dominant mode simultaneously, it is classified as type 2, as shown in Figure 2(c1,c2).

It is known that one typical feature of EEs is the long tail in the probability density function (PDF), which describes the probability of different pulse intensities [8,17]. In Figure 3a, we plot the PDF of peak intensities in I_{total} in log-scale. The function clearly deviates from a Gaussian distribution at large intensity, similar to those trends in Refs. [18,19,30]. Besides, we measure the waiting time between two consecutive EEs on the log-scale $\log(t_{i+1}/t_i)$, as shown in Figure 3b. The two dashed fitting curves reveal that continuous EEs with low and large time intervals follow two different Poisson laws with different slopes, in which the optical feedback introduces a new law at short waiting times. It is also easily understood that there are more EEs at higher feedback strengths, which leads to more EEs and a significant increase in the slope at short waiting times [14]. Further, we also draw the waiting time between two consecutive type 1 EEs [Figure 3c] or type 2 EEs [Figure 3d]. The trends in Figure 3c,d are notably similar, though the count in the latter is higher due to the greater number of type 2 EEs. Thus, we will investigate the numerical characteristics of EEs below.

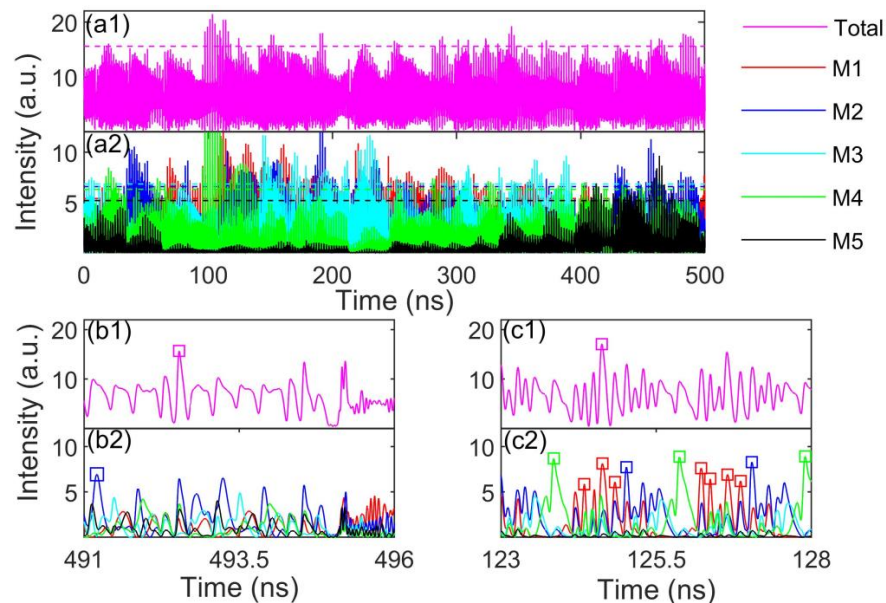


Figure 2. (a1,a2) Intensity time series, where $k_f = 30 \text{ ns}^{-1}$, $\tau_f = 2 \text{ ns}$. The dashed lines represent the threshold of $AI = 2$. (b1,b2,c1,c2) Zoom of time series presented in panels (a1), and the colored squares mark EEs in corresponding output.

In the optical feedback laser system, the feedback strength k_f is a very critical parameter, so we then discuss the effect of the feedback strength on EEs in the multimode laser. Herein, we plot the DMR of the five modes as a function of k_f in Figure 4a. We find that the DMR curve of the central mode (M3) is higher than that of other modes, and the DMR curve of the mode closer to the central mode is higher. The phenomenon can be understood

as follows: the central mode obtains the maximum gain in the medium, and the further from the central mode, the smaller gain is obtained, which correspondingly results in a decreasing output intensity. In Figure 4b, the relative number of EEs (the ratio between the number of EEs and the number of peaks in the time series) in the modes and the total time series are calculated. The relative number of EEs in I_{total} first increases slowly for $k_f < 25 \text{ ns}^{-1}$, then decreases for $k_f \in [25, 32 \text{ ns}^{-1}]$, and finally approaches 2.5% with larger k_f . While the relative number of EEs in $I_{M1,M2,M3,M4,M5}$ tends to be saturated, about 3~4%, in a large range of k_f . By further comparing Figure 4a,b, we know that DMR is lower for the whole parameter range in $I_{M1,M5}$, but the relative number of EEs is larger, and the relative number of EEs in I_{total} (the maximum output) is significantly smaller than that of each mode.

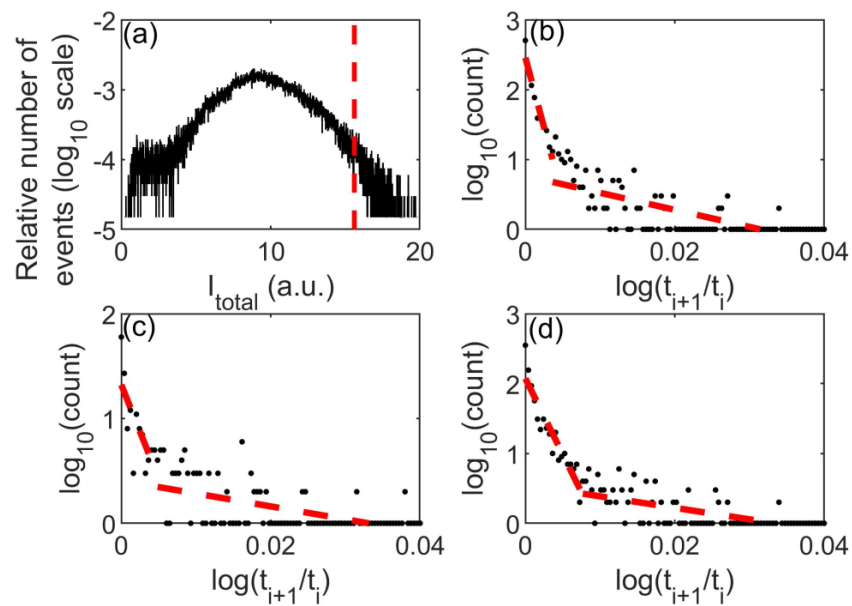


Figure 3. (a) The PDF of the time series in Figure 2(a1), where the dashed line represents the threshold of AI. (b) Waiting times between consecutive EEs in I_{total} , for either (c) type 1 or (d) type 2. The dashed lines are fitting curves.

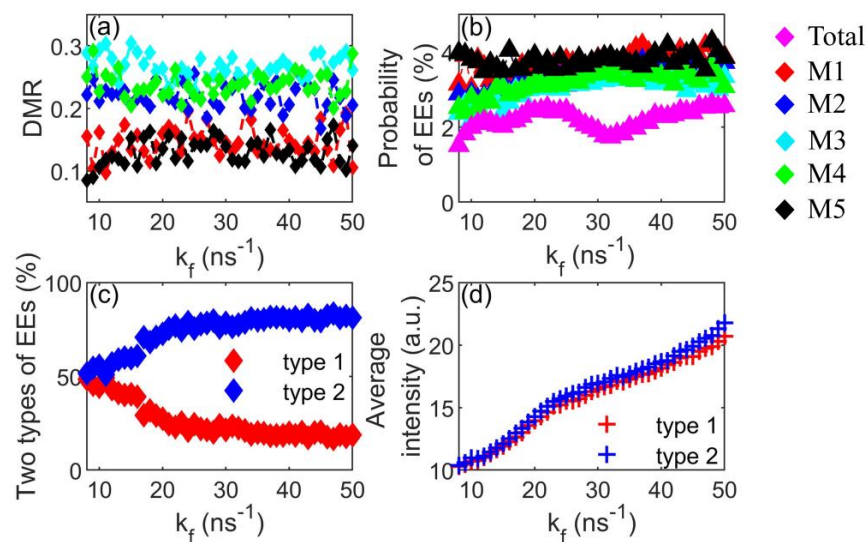


Figure 4. (a) DMR of the five modes as a function of k_f , (b) relative number of EEs in I_{total} and $I_{M1,M2,M3,M4,M5}$, (c) relative number of two types of EEs in I_{total} , and (d) average intensity of the two types of EEs. The feedback delay is set at $\tau_f = 2 \text{ ns}$.

Next, we investigate the evolution of two types of EEs as classified above. In Figure 4c, we present the relative number of the two kinds of EEs as a function of k_f . It is worth noting that the relative numbers are close to each other at first, then the proportion of type 1 EEs (marked in red) slowly decreases for $k_f < 16 \text{ ns}^{-1}$, while the decreasing trend becomes sharper for $k_f \in [16, 25 \text{ ns}^{-1}]$, and finally tends to be about 18% for larger k_f . The evolution of type 2 EEs is completely opposite to that of type 1 EEs. Besides, we also take into account the effect of k_f on the average intensity of the two types of EEs, as shown in Figure 4d. Obviously, the intensity of both EEs increases with increasing k_f , and the trends of both are similar. Although the intensity of both EEs is very close for small k_f , the magnitude of type 2 EEs (marked in blue) dominates for larger k_f . These results reveal that k_f plays an important role in controlling the EE generation rate. Especially, the presence of two kinds of EEs can be controlled by adjusting k_f .

To gain a global view of the effects of feedback parameters on the EE evolution, we plot the relative number maps in the (k_f, τ_f) plane, as shown in Figure 5, where colors represent the relative number of EEs in I_{total} and $I_{M1, M2, M3, M4, M5}$. Note that the white corresponds to non-chaotic regions and the gray to chaotic regions. In Figure 5a, we find that the relative number of EEs in I_{total} is about 2~3% in almost the whole parameter space, supporting chaos. However, maps of the central mode I_{M3} [Figure 5d], I_{M2} [Figure 5c], and I_{M4} [Figure 5e] show a similar trend: the relative number of EEs is 2~3% for $k_f < 20 \text{ ns}^{-1}$, while the relative number of EEs can increase to 3~4% for larger k_f . Besides, maps of I_{M1} [Figure 5b] and I_{M5} [Figure 5f] have wider and darker red regions, representing a larger relative number (about 4~5%) and stabler saturation. It is worth noting that the relative number of EEs for each mode is always larger than that of I_{total} , which reveals that the trend observed in Figure 4b holds true within the selected feedback delay range.

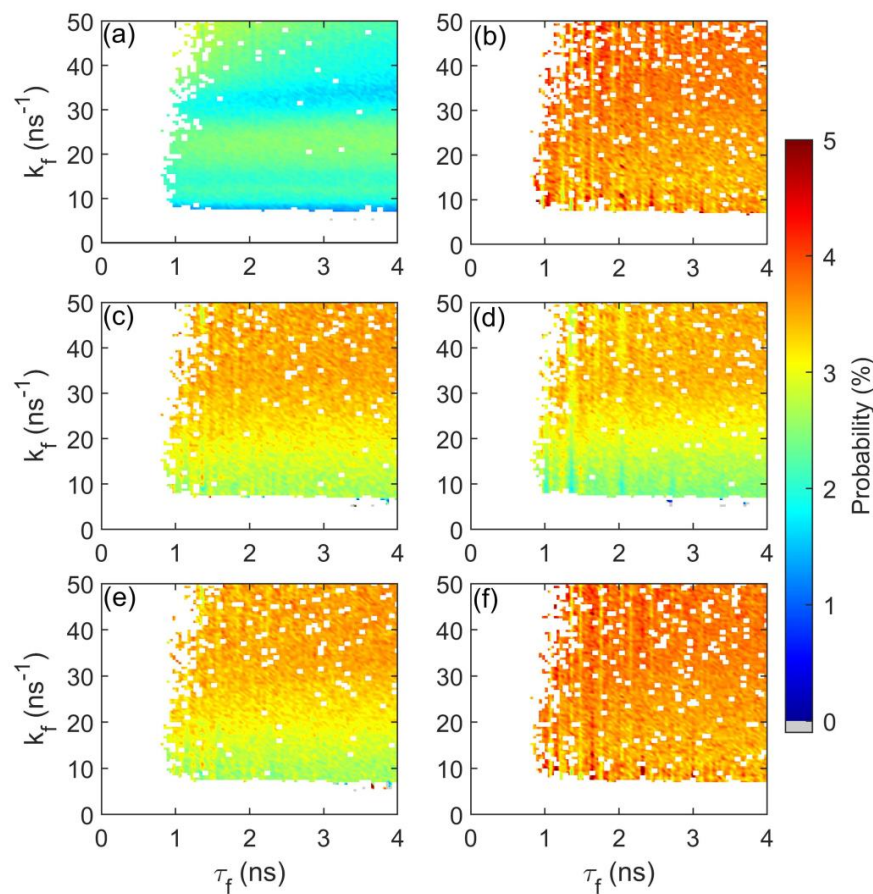


Figure 5. Maps of the relative number of EEs in the (k_f, τ_f) plane. (a) for I_{total} , and (b–f) for $I_{M1}, I_{M2}, I_{M3}, I_{M4}$, and I_{M5} , respectively. Here, the EE is defined by $AI = 2$, and $I/I_{th} = 2$.

The pump current is also a key parameter for the appearance of EEs; thus, we draw maps of the relative number of EEs in the $(k_f, I/I_{th})$ plane. Likewise, the white represents non-chaotic regions. In Figure 6, we are surprised to discover that the relative number of EEs is larger in the chaotic parameter regions under smaller pump current, both for the total output and for the five modes. Compared with Figure 5, although I_{M2} , I_{M3} , and I_{M4} still tend to be saturated, the critical k_f varies greatly for different currents in Figure 6. It is also easy to understand that the larger current will increase the average intensity of the time series, thus requiring greater optical feedback strength to interact with the light in the cavity and reach saturation. In addition, there are some phenomena similar to those in Figure 5. For example, the evolution trends of the relative number of EEs in the two-dimensional maps of I_{M2} [Figure 6c], I_{M3} [Figure 6d], and I_{M4} [Figure 6e] are similar, while I_{M1} [Figure 6b] and I_{M5} [Figure 6f] also evolve similarly, and the relative number of EEs in these modes is always larger than that in I_{total} .

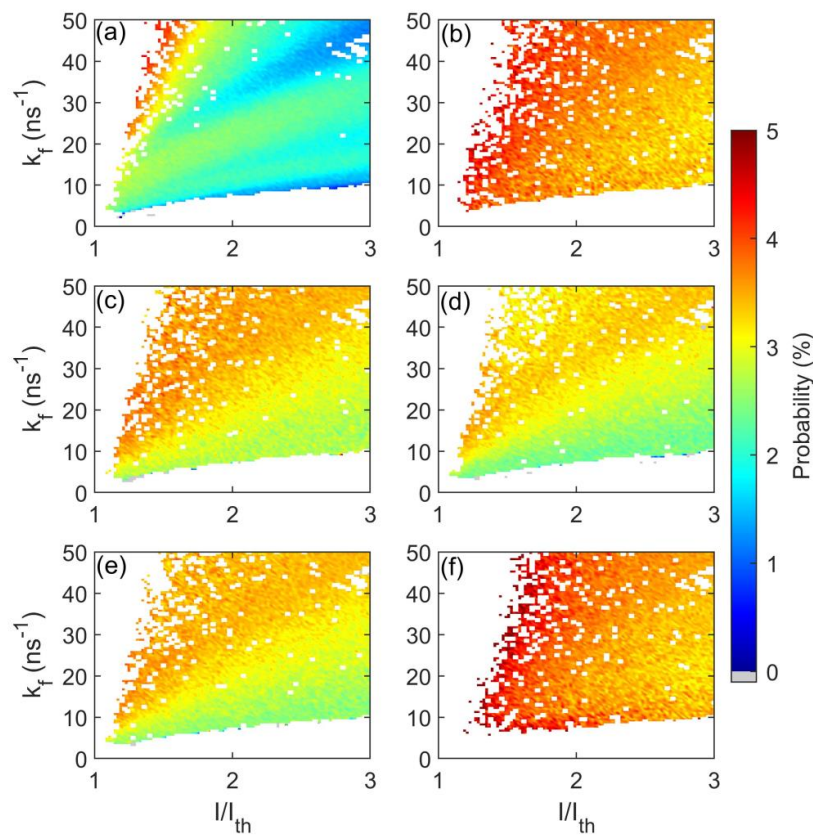


Figure 6. Maps of the relative number of EEs in the $(k_f, I/I_{th})$ plane. (a) for I_{total} , and (b–f) for I_{M1} , I_{M2} , I_{M3} , I_{M4} , and I_{M5} , respectively. Here the EE is defined by $AI = 2$, and the feedback delay is set at 2 ns.

3.2. Another Threshold Definition of EEs

Considering the criterion given by the threshold of $AI = 2$ is relatively low, we will discuss EEs in this section using a stricter criterion, i.e., $\langle H \rangle + 5\sigma$. The more detailed typical time series of Figure 2 and the corresponding PDFs are again given in Figure 7. The relative numbers of EEs calculated under two standards are listed in Table 1. The red dashed line in Figure 7 represents the threshold of $AI = 2$, and the black dashed line is the threshold of $\langle H \rangle + 5\sigma$. It can be clearly seen that the latter threshold is more stringent than the former, and some EEs determined by the former are excluded by the latter, which also explains that the relative number of EEs defined by the latter definition is one or even two orders of magnitude smaller than the former. In Figure 7(a2–f2), the individual modes have a more pronounced long tail than I_{total} , and thus EEs can be detected under the stricter standard.

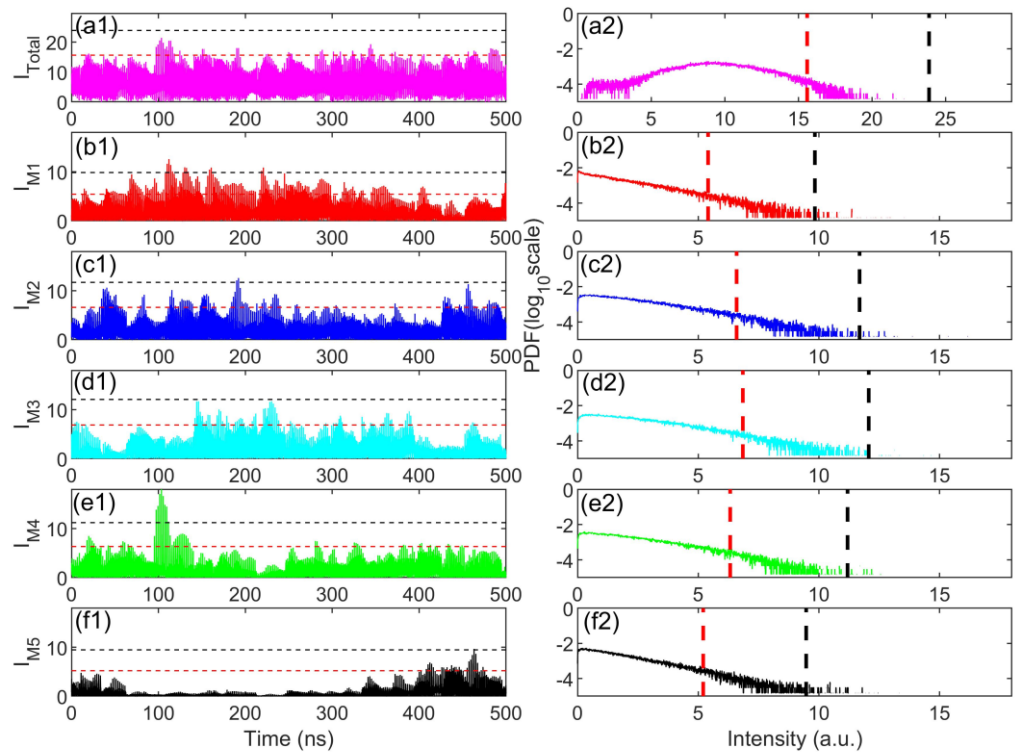


Figure 7. Intensity time series of total output (a1) and mode 1–mode 5 (b1–f1), and (a2–f2) are the corresponding PDFs. The red dashed lines represent the threshold of $AI = 2$, and the black ones stand for the threshold of $\langle H \rangle + 5\sigma$. The other parameters are the same as those in Figure 2.

Table 1. Comparison of the relative number of EEs under the two criteria.

Output	Threshold $AI = 2$	Threshold $\langle H \rangle + 5\sigma$
I_{total}	1.90%	0.00%
I_{M1}	3.83%	0.11%
I_{M2}	3.43%	0.07%
I_{M3}	3.27%	0.05%
I_{M4}	3.45%	0.07%
I_{M5}	3.81%	0.17%

We also plot the maps of the relative number of EEs defined by $\langle H \rangle + 5\sigma$ in the (k_f, τ_f) plane (Figure 8) or in the $(k_f, I/I_{th})$ plane (Figure 9). Likewise, white represents the non-chaotic state, and gray corresponds to the chaotic state. Then, we calculate the relative number of EEs and color in the gray areas. In Figure 8a, there are large regions of gray with only scattered patches of blue, which means that few EEs or even no EEs are detected in I_{total} . Maps of the central mode I_{M3} [Figure 8d], I_{M2} [Figure 8c], and I_{M4} [Figure 8e] still show trends similar to those in Figure 5, but in much smaller relative numbers. I_{M1} [Figure 8b] and I_{M5} [Figure 8f], however, have different behaviors from the cases considered before in Figure 5. Specifically, they show a tendency to increase before saturation, similar to the other three modes. We speculate that the previous threshold of $AI = 2$ classifies some moderate-intensity pulses as EEs, resulting in an indistinct trend in the evolution of EEs. After careful comparison among Figures 5, 6, 8 and 9, the EE trends defined by the stricter threshold of $\langle H \rangle + 5\sigma$ are basically similar to those defined by the threshold $AI = 2$, except for the one mentioned above.

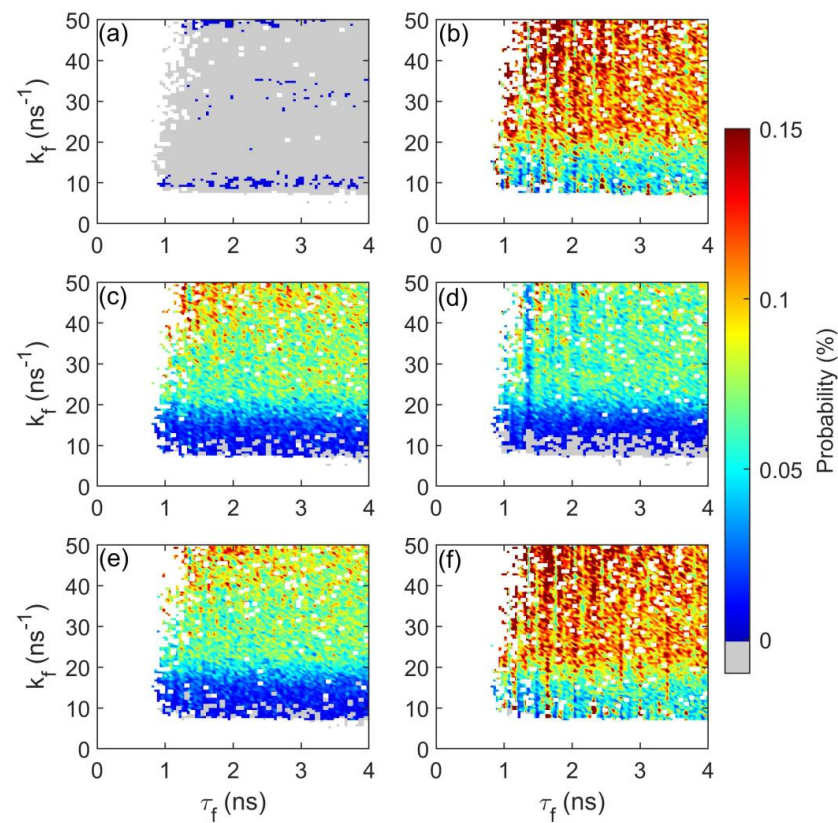


Figure 8. Maps of the relative number of EEs in the (k_f, τ_f) plane. (a) for I_{total} , and (b–f) for $I_{M1}, I_{M2}, I_{M3}, I_{M4}$, and I_{M5} , respectively. Here the EE is defined by $\langle H \rangle + 5\sigma$, and $I/I_{th} = 2$.

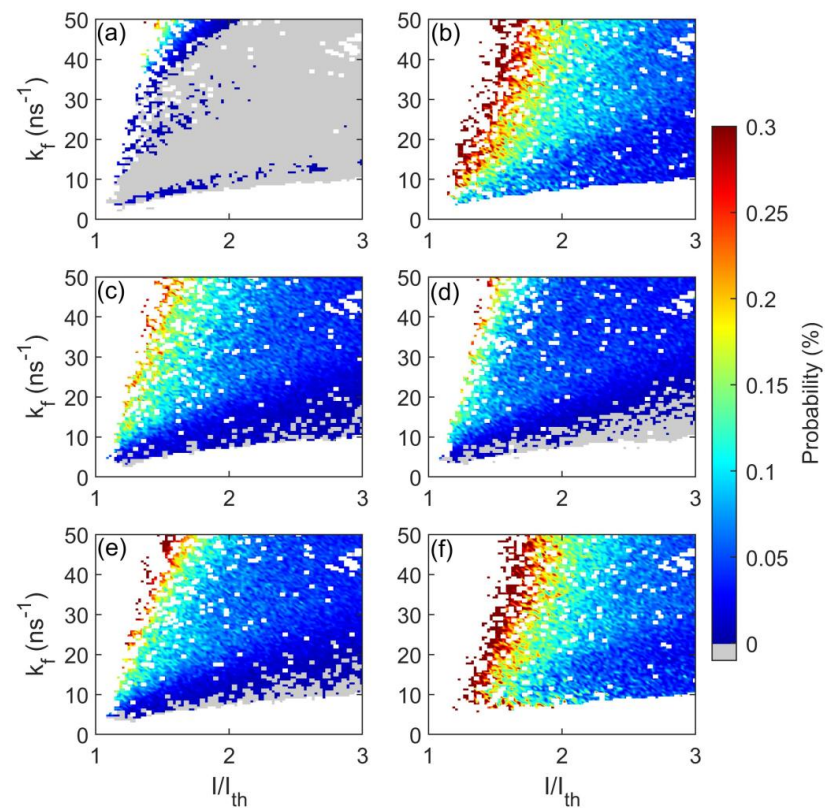


Figure 9. Maps of the relative number of EEs in the $(k_f, I/I_{th})$ plane. (a) for I_{total} , and (b–f) for $I_{M1}, I_{M2}, I_{M3}, I_{M4}$, and I_{M5} , respectively. Here the EE is defined by $\langle H \rangle + 5\sigma$, and $\tau_f = 2$ ns.

4. Conclusions

In summary, we have investigated the evolution of EEs in an FP laser with optical feedback. Some interesting phenomena can be revealed. Firstly, EEs can be observed in both the total intensity I_{total} and the individual mode intensity $I_{M1,M2,M3,M4,M5}$, where the pulse amplitude is higher than the threshold of $AI = 2$ and the PDF emerges as a long tail. Particularly, we divide the EEs of I_{total} into two types based on whether EEs are generated in the dominant mode simultaneously. We also discuss the evolution of all EEs and two types of EEs with increasing feedback strength and find a clear saturation trend. Finally, we analyze the effects of key parameters, i.e., the feedback strength, feedback delay, and pump current, on the probability of EEs by plotting two-dimensional maps under two threshold criteria for EEs. We hope that this work can motivate more research on EEs in various multimode lasers. In addition, we believe that the study of EEs in F-P laser systems can optimize system performance in a variety of applications based on chaotic signals generated from F-P lasers, such as secure communications.

Author Contributions: Conceptualization and resources, N.L.; simulation, S.G., K.L. and Y.H.; supervision, X.Z. and N.L.; all authors contributed to the writing of the manuscript. Y.H. and N.L. contributed to the review of the manuscript. All authors have read and agreed to the published version of the manuscript.

Funding: This study was funded by National Natural Science Foundation of China (62171305); Innovative and Entrepreneurial Talent Program of Jiangsu Province (JSSCRC2021527); the Natural Science Research Project of Jiangsu Higher Education Institutions of China (23KJA51007). The Postdoctoral Fellowship Program of CPSF (GZC20231883).

Institutional Review Board Statement: Not applicable.

Informed Consent Statement: Not applicable.

Data Availability Statement: Data underlying the results presented in this paper are not publicly available at this time but may be obtained from the authors upon reasonable request.

Conflicts of Interest: Xin Zhu was employed by the Matrix Opto. Co., Ltd. Other authors declare no conflicts of interest.

References

1. Broad, W.J. Rogue giants at sea. *The New York Times*, 11 July 2006; p. 11.
2. Yan, Z.-Y. Financial rogue waves. *Commun. Theor. Phys.* **2010**, *54*, 947. [[CrossRef](#)]
3. Efimov, V.; Ganshin, A.; Kolmakov, G.; McClintock, P.; Mezhov-Deglin, L. Rogue waves in superfluid helium. *Eur. Phys. J. Spec. Top.* **2010**, *185*, 181–193. [[CrossRef](#)]
4. Ganshin, A.; Efimov, V.; Kolmakov, G.; Mezhov-Deglin, L.; McClintock, P.V. Observation of an inverse energy cascade in developed acoustic turbulence in superfluid helium. *Phys. Rev. Lett.* **2008**, *101*, 065303. [[CrossRef](#)] [[PubMed](#)]
5. Wang, W.-X.; Yang, R.; Lai, Y.-C.; Kovanis, V.; Grebogi, C. Predicting catastrophes in nonlinear dynamical systems by compressive sensing. *Phys. Rev. Lett.* **2011**, *106*, 154101. [[CrossRef](#)] [[PubMed](#)]
6. Tlidi, M.; Taki, M. Rogue waves in nonlinear optics. *Adv. Opt. Photon.* **2022**, *14*, 87–147. [[CrossRef](#)]
7. Dudley, J.M.; Genty, G.; Mussot, A.; Chabchoub, A.; Dias, F. Rogue waves and analogies in optics and oceanography. *Nat. Rev. Phys.* **2019**, *1*, 675–689. [[CrossRef](#)]
8. Solli, D.R.; Ropers, C.; Koonath, P.; Jalali, B. Optical rogue waves. *Nature* **2007**, *450*, 1054–1057. [[CrossRef](#)]
9. Xu, J.M.; Wu, J.; Ye, J.; Song, J.X.; Yao, B.C.; Zhang, H.W.; Leng, J.Y.; Zhang, W.L.; Zhou, P.; Rao, Y.J. Optical rogue wave in random fiber laser. *Photon. Res.* **2020**, *8*, 1–7. [[CrossRef](#)]
10. Pammi, V.A.; Clerc, M.G.; Coulibaly, S.; Barbay, S. Extreme events prediction from nonlocal partial information in a spatiotemporally chaotic microcavity laser. *Phys. Rev. Lett.* **2023**, *130*, 223801. [[CrossRef](#)]
11. Teğin, U.; Wang, P.; Wang, L.V. Real-time observation of optical rogue waves in spatiotemporally mode-locked fiber lasers. *Commun. Phys.* **2023**, *6*, 60. [[CrossRef](#)]
12. Wu, X.; Zhang, Y.; Peng, J.; Boscolo, S.; Finot, C.; Zeng, H. Control of spectral extreme events in ultrafast fiber lasers by a genetic algorithm. *Laser Photonics Rev.* **2023**, *18*, 2200470. [[CrossRef](#)]
13. Wang, T.; Zhou, H.; Fang, Q.; Han, Y.; Guo, X.; Zhang, Y.; Qian, C.; Chen, H.; Barland, S.; Xiang, S.; et al. Reservoir computing-based advance warning of extreme events. *Chaos Solitons Fract.* **2024**, *181*, 114673. [[CrossRef](#)]
14. Mercier, E.; Even, A.; Mirisola, E.; Wolfersberger, D.; Sciamanna, M. Numerical study of extreme events in a laser diode with phase-conjugate optical feedback. *Phys. Rev. E* **2015**, *91*, 042914. [[CrossRef](#)]

15. Spitz, O.; Wu, J.; Herdt, A.; Maisons, G.; Carras, M.; Elsässer, W.; Wong, C.-W.; Grillot, F. Extreme events in quantum cascade lasers. *Adv. Photonics* **2020**, *2*, 066001. [[CrossRef](#)]
16. Coulibaly, S.; Clerc, M.G.; Selmi, F.; Barbay, S. Extreme events following bifurcation to spatiotemporal chaos in a spatially extended microcavity laser. *Phys. Rev. A* **2017**, *95*, 023816. [[CrossRef](#)]
17. Bonatto, C.; Feyereisen, M.; Barland, S.; Giudici, M.; Masoller, C.; Leite, J.R.; Tredicce, J.R. Deterministic optical rogue waves. *Phys. Rev. Lett.* **2011**, *107*, 053901. [[CrossRef](#)] [[PubMed](#)]
18. Uy, C.H.; Rontani, D.; Sciamanna, M. Vectorial extreme events in VCSEL polarization dynamics. *Opt. Lett.* **2017**, *42*, 2177–2180. [[CrossRef](#)] [[PubMed](#)]
19. Zeng, Y.; Zhou, P.; Huang, Y.; Li, N. Extreme events in optically pumped spin-VCSELs. *Opt. Lett.* **2022**, *47*, 142–145. [[CrossRef](#)]
20. Iwami, R.; Mihana, T.; Kanno, K.; Sunada, S.; Naruse, M.; Uchida, A. Controlling chaotic itinerancy in laser dynamics for reinforcement learning. *Sci. Adv.* **2022**, *8*, eabn8325. [[CrossRef](#)]
21. Bogris, A.; Mesaritakis, C.; Deligiannidis, S.; Li, P. Fabry-Perot lasers as enablers for parallel reservoir computing. *IEEE J. Sel. Top. Quantum Electron.* **2021**, *27*, 7500307. [[CrossRef](#)]
22. Gao, H.; Wang, A.; Wang, L.; Jia, Z.; Guo, Y.; Gao, Z.; Yan, L.; Qin, Y.; Wang, Y. 0.75 Gbit/s high-speed classical key distribution with mode-shift keying chaos synchronization of Fabry-Perot lasers. *Light Sci. Appl.* **2021**, *10*, 172. [[CrossRef](#)] [[PubMed](#)]
23. Xiang, S.; Shi, Y.; Guo, X.; Zhang, Y.; Wang, H.; Zheng, D.; Song, Z.; Han, Y.; Gao, S.; Zhao, S.; et al. Hardware-algorithm collaborative computing with photonic spiking neuron chip based on an integrated Fabry-Perot laser with a saturable absorber. *Optica* **2023**, *10*, 162–171. [[CrossRef](#)]
24. Lang, R.; Kobayashi, K. External optical feedback effects on semiconductor injection laser properties. *IEEE J. Quantum Electron.* **1980**, *16*, 347–355. [[CrossRef](#)]
25. Han, H.; Zhang, M.J.; Shore, K.A. Chaos bandwidth enhancement of Fabry-Perot laser diode with dual-mode continuous-wave optical injection. *IEEE J. Quantum Electron.* **2019**, *55*, 2000708. [[CrossRef](#)]
26. Iwami, R.; Kanno, K.; Uchida, A. Chaotic mode-competition dynamics in a multimode semiconductor laser with optical feedback and injection. *Opt. Express* **2023**, *31*, 11274–11291. [[CrossRef](#)] [[PubMed](#)]
27. Huang, Y.; Zhou, P.; Zeng, Y.; Zhang, R.; Li, N. Evolution of extreme events in a semiconductor laser subject to chaotic optical injection. *Phys. Rev. A* **2022**, *105*, 043521. [[CrossRef](#)]
28. Dal Bosco, A.K.; Wolfersberger, D.; Sciamanna, M. Extreme events in time-delayed nonlinear optics. *Opt. Lett.* **2013**, *38*, 703–705. [[CrossRef](#)] [[PubMed](#)]
29. Reinoso, J.A.; Zamora-Munt, J.; Masoller, C. Extreme intensity pulses in a semiconductor laser with a short external cavity. *Phys. Rev. E* **2013**, *87*, 062913. [[CrossRef](#)] [[PubMed](#)]
30. Zeng, Y.; Huang, Y.; Zhou, P.; Mu, P.; Li, N. Controlling the likelihood of extreme events in an optically pumped spin-VCSEL via chaotic optical injection. *Opt. Express* **2023**, *31*, 16178–16191. [[CrossRef](#)]
31. Li, X.-Z.; Zhou, X.; Gu, Y.; Zhao, M. Numerical study of statistical properties for semiconductor laser chaos by exploring the injection parameter space. *IEEE J. Sel. Top. Quantum Electron.* **2022**, *28*, 0600108. [[CrossRef](#)]

Disclaimer/Publisher’s Note: The statements, opinions and data contained in all publications are solely those of the individual author(s) and contributor(s) and not of MDPI and/or the editor(s). MDPI and/or the editor(s) disclaim responsibility for any injury to people or property resulting from any ideas, methods, instructions or products referred to in the content.